



ÉCOLE POLYTECHNIQUE FÉDÉRALE DE LAUSANNE

**Towards replicating the full chewing process : Initial
development of a Stewart platform-based chewing
robot.**

MASTER THESIS

Author :

Barbara DE GROOT, 296815

CREATE Lab, Prof. Josie Hughes

Supervisor : Benhui Dai

June 17, 2025

Contents

1	Introduction	3
2	Methods	4
2.1	Design requirements from human physiology	4
2.2	Mechanical design	4
2.2.1	6 DoF mechanism selection	4
2.2.2	Actuator requirements and selection	5
2.2.3	Jaw subassemblies	7
2.2.4	Full assembly	7
2.3	Control	9
2.3.1	Hardware (electronics)	9
2.3.2	Software architecture	10
2.3.3	Stewart platform control	11
2.3.4	Force sensing	13
2.4	Data acquisition and processing	14
2.4.1	Subjects	14
2.4.2	Motion-capture acquisition	14
2.4.3	Data processing	15
3	Results	16
3.1	Mimicking human jaw motion	16
3.2	Motion captured chewing trajectories	16
3.3	Position control	16
3.4	Force analysis	18
3.4.1	Maximum force	18
3.4.2	Force feedback distribution	18
4	Discussion	19
4.1	Summary of findings	19
4.2	Limitations	19
4.3	Future work	19
5	Conclusion	20

6	References	21
7	Appendix	22

1 Introduction

Human chewing is a complex process, involving different systems such as the jaw, teeth, tongue and saliva, all coordinated to break down food into a bolus that can be swallowed and digested. Chewing robots are a great tool to study this process that is not yet fully understood as they give us the opportunity for a closely controlled environment where each parameter can be adjusted and measured. This makes them valuable not only for advancing our understanding of chewing mechanics and related disorders, but also for a wide range of applications. In dentistry, they are used to test how implants and other dental devices wear over time. In food science, they help assess texture and flavor release during mastication. They also offer a reliable platform for studying the release of active compounds in chewable medications such as medical chewing gum.

Nowadays, many mastication robots exist, and while most are limited in their ability to fully mimic human chewing due to restricted degrees of freedom, some have already made significant progress. For example, the Bristol Dento-Munch Robo-Simulator [1] features 6 degrees of freedom (DoF), closed-loop control, force feedback, and a full set of teeth capable of replicating human chewing forces. Similarly, the robot developed by Seung-Ju et al. [2] offers the same capabilities, with a design that matches more closely human biomechanics. Another system, by Alemzadeh et al. [3], includes a closed mouth and artificial saliva—two important components of realistic mastication—even though it has limited sensory feedback. However, no existing system combines all critical elements: 6 DoF, position and multidirectional force feedback, a hermetically closed mouth with saliva circulation, and an actuated tongue. Without them it is not possible to accurately reproduce the entire chewing process. For example, without a tongue, the robot cannot direct the food towards the teeth during chewing or without saliva, the food cannot be mixed with enzymes that aid digestion. This greatly limits what kind of chewing experiments can be performed, as well as the robot’s ability to adapt to different food types and textures.

This project addresses that gap by taking the first step toward an all-inclusive chewing robot. Because only four months were available and no previous hardware existed, the present work concentrates on the mechanical foundation: a modular 6-DoF Stewart platform-based jaw sized from physiological data, equipped with tri-axial force sensing and position feedback. The overarching research question is therefore narrowed to:

How can a modular Stewart-platform jaw be designed and validated so that it reproduces human chewing trajectories and forces while exposing interfaces for future tongue and saliva modules?

To answer this question, we (i) designed and built the platform, (ii) implemented a simple closed-loop control system that can be scaled in later iterations, (iii) recorded our own motion-capture dataset of human chewing, and (iv) replayed these trajectories on the robot to assess its performance. By laying down a flexible, expandable foundation, this work enables future integration of artificial saliva flow, an artificial tongue and adaptive bio-inspired control, moving one step closer to a robot that replicates the complete human chewing process.

2 Methods

2.1 Design requirements from human physiology

The jaw makes essential contributions to the chewing process such as generating the forces required to break down food, controlling the lower mandible motion and giving sensory feedback. A robotic jaw should therefore be able to mimic these functions as closely as possible. As this is the first iteration of the chewing robot, we focus on force generation and range of motion, while sensory feedback and other functions can be added in future iterations. The design requirements are based on the literature and the human jaw anatomy and physiology, as summarized in Table 1. Note that the jaw’s speed is not a design requirement as food can be effectively chewed even at slow speeds.

Quantity	Values reported in the literature	Design requirement
Degrees of freedom (DoF)	6 DoF: 3 translational (X, Y, Z) and 3 rotational (roll, pitch, yaw) [4]	6 DoF
Vertical (compressive) bite force F_z	600 N chewing force in healthy adults [5], 1243 N maximum clenching force [6]	800 N
Lateral force F_x	−72 N (left) to +53 N (right) during maximal biting [7]	±100 N
Anterior–posterior force F_y	−10 N (posterior) to +30 N (anterior) [7]	±50 N
Mandibular motion range	14 mm lateral shift, 11 mm protrusion, 61 mm mouth opening in healthy adults [8]	±20 mm (X, Y); 0–70 mm (Z)

Table 1: Functional design requirements.

2.2 Mechanical design

This section details the key design decisions that led to the final mechanical design of the chewing robot and the resulting specifications.

2.2.1 6 DoF mechanism selection

The first major design decision was how to achieve 6 degrees of freedom (DoF) for jaw motion. In the field of robotic mastication, two common approaches are used. The first is a biomechanically inspired design using linear actuators [2] or combinations of actuated cables and springs [3] to replicate muscle behavior. The second is a Stewart platform [1]—a widely used 6-DoF parallel mechanism, often seen in motion simulators. See Figure 1 for a visualization of the two approaches.

For this project, we chose the Stewart platform approach. Its well-defined kinematics and ease of control make it particularly suitable for our goal of replicating recorded human chewing motion. Because our control strategy is based on reproducing real motion trajectories, having a platform with straightforward inverse kinematics is a key advantage.

Stewart platforms generally come in two configurations: one based on rotary servo motors and

one based on linear actuators, see Figure 1. We selected the linear actuator design for several reasons. It offers more efficient force transmission, a simpler kinematic model, and greater structural rigidity—all important factors when attempting to reproduce the forces involved in human chewing.

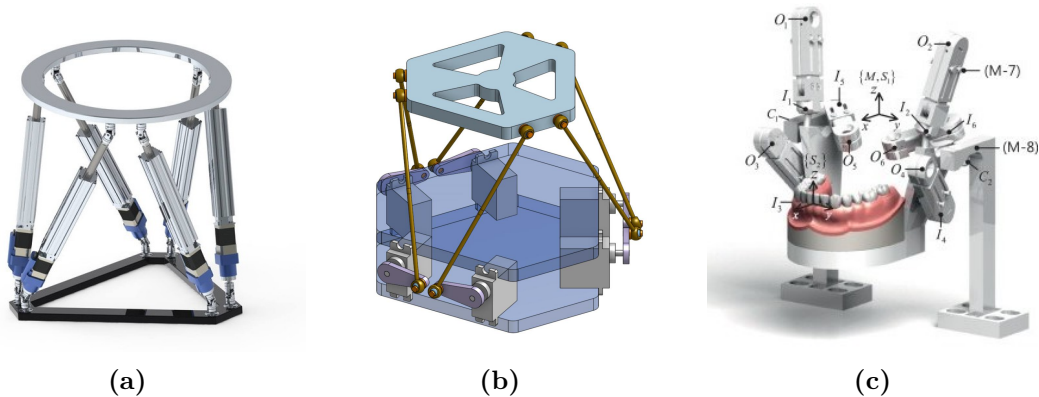


Figure 1: (a) Linear actuator-based Stewart platform. (b) Rotary servo motor-based Stewart platform. (c) Biomechanically inspired robotic jaw design[2].

2.2.2 Actuator requirements and selection

The combination of high bite-force replication and position feedback demands actuators large enough to deliver both power and sensing hardware; their size therefore becomes a critical design constraint. Their stroke and force requirements are fixed by the functional criteria in Table 1.

Design assumptions. To compute the required actuator specifications, we assumed a minimum actuator mounting angle of at least 45° to the horizontal and the general geometry of the platform and base shown in Figure 2.

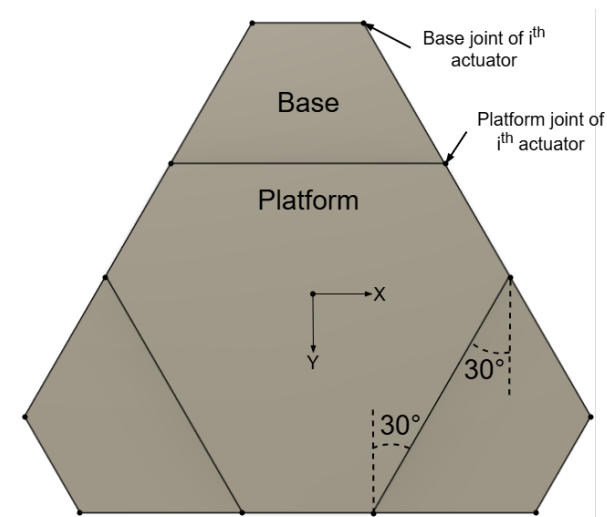


Figure 2: Top view of the base and platform design assumption.

Stroke length. Guided by the workspace analysis from Masory et al. [9], we prioritize achieving the necessary vertical range of motion, knowing that sufficient horizontal range would follow.

The minimum required stroke length is:

$$l_{\min} = \frac{z_{\max} - z_{\min}}{\sin(45^\circ)} = \frac{70 \text{ mm}}{\sin(45^\circ)} \approx 99 \text{ mm} \quad (1)$$

Load. To meet the minimum vertical force requirement of 800 N, each actuator must provide a load of at least:

$$F_{\min} = \frac{F_{z,\min}}{6 \cdot \sin(45^\circ)} = \frac{800 \text{ N}}{6 \cdot \sin(45^\circ)} \approx 189 \text{ N} \quad (2)$$

With this minimum actuator force, we estimate the lateral (shear) and front-back force capacities as:

$$F_x \approx 2 \cdot \cos(45^\circ) \cdot F_{\min} + 4 \cdot \cos(45^\circ) \cdot \sin(30^\circ) \cdot F_{\min} \approx 534 \text{ N} \gg 100 \text{ N} \quad (3)$$

$$F_y \approx 4 \cdot \cos(45^\circ) \cdot \cos(30^\circ) \cdot F_{\min} \approx 462 \text{ N} \gg 50 \text{ N} \quad (4)$$

These calculations show that ensuring the vertical force requirement is met also guarantees that shear forces in the x and y directions will exceed their respective targets.

Speed and feedback. Since speed is not a strict requirement for this prototype, we prioritized force over velocity when selecting actuators. Position feedback is necessary for closed-loop control, as we use inverse kinematics to compute actuators lengths based on the desired platform pose.

Selection. We selected the PA-14P-4-50 linear actuator, which meets both stroke and force requirements as seen in Table 2. The dimensions of both base and platform, see Figure 3, were chosen to accommodate the size of the actuators. The resulting vertical workspace of the platform is 118 mm, which is more than enough to cover the required 70 mm.

At mid-stroke, the actuators are positioned at an angle of 60° relative to the horizontal plane. Under this configuration, the theoretical maximum force outputs are: $F_{z,\max} = 1155 \text{ N}$ (vertical), $F_{x,\max} = 444 \text{ N}$ (lateral), and $F_{y,\max} = 385 \text{ N}$ (anterior-posterior). All values surpass the design requirements specified in Table 1. These are idealized values and do not account for frictional losses or mechanical inefficiencies.

Parameter	Value
Stroke length	101 mm
Max force	222.4 N
Speed (no load)	28 mm/s
Speed (full load)	21 mm/s
Position feedback	Potentiometer
Protection class	IP54
Power supply	12 V DC

Table 2: PA-14P-4-50 specifications.

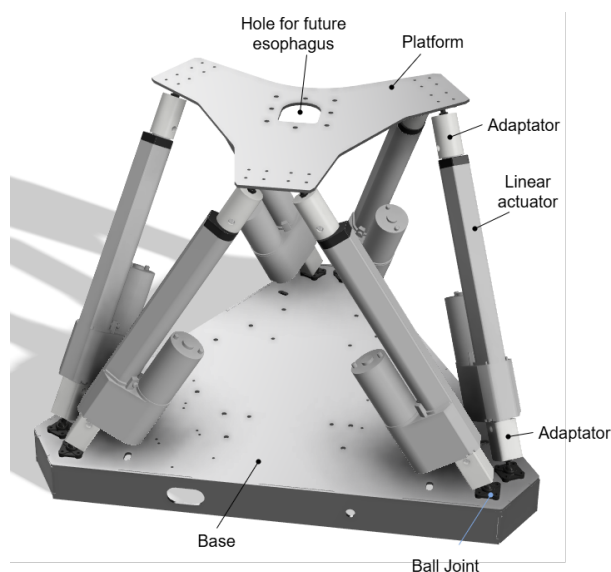


Figure 3: Final Stewart platform design.

2.2.3 Jaw subassemblies

Next, we designed the lower and upper jaws, which are attached to the platform and base respectively.

Lower jaw. The lower jaw, Figure 4a, is mounted on the moving platform and elevated using four aluminum rods. This elevation provides two main advantages: it creates a clear line of sight to place a motion capture marker on the gnathion, and it leaves space beneath the jaw for integrating a future esophagus module. The mandibular teeth are fixed to a rigid plate and positioned slightly forward to leave room for a future tongue module. This plate already accomodates a hole for a future esophagus module.

Upper jaw. The upper jaw, Figure 4b, is mounted on a rigid frame made of aluminum rods to ensure sufficient stability and stiffness under loading. This rigidity is essential to resist the forces applied by the lower jaw during chewing. Three-axis load cells are installed on the upper jaw mounting plate to measure both vertical and lateral forces during contact. Two acrylic adaptor plates connect these load cells to the maxillary teeth. The top adaptor has a central opening reserved for a future camera, which will be used to observe food behavior during mastication.

Exchangeable teeth. Both the maxillary and mandibular teeth are designed to be easily replaceable through the use of acrylic adaptor plates. This modularity allows for testing different tooth shapes, materials, and conditions (e.g., healthy, aged, or damaged teeth), which will be important for future studies on chewing development and masticatory disorders.

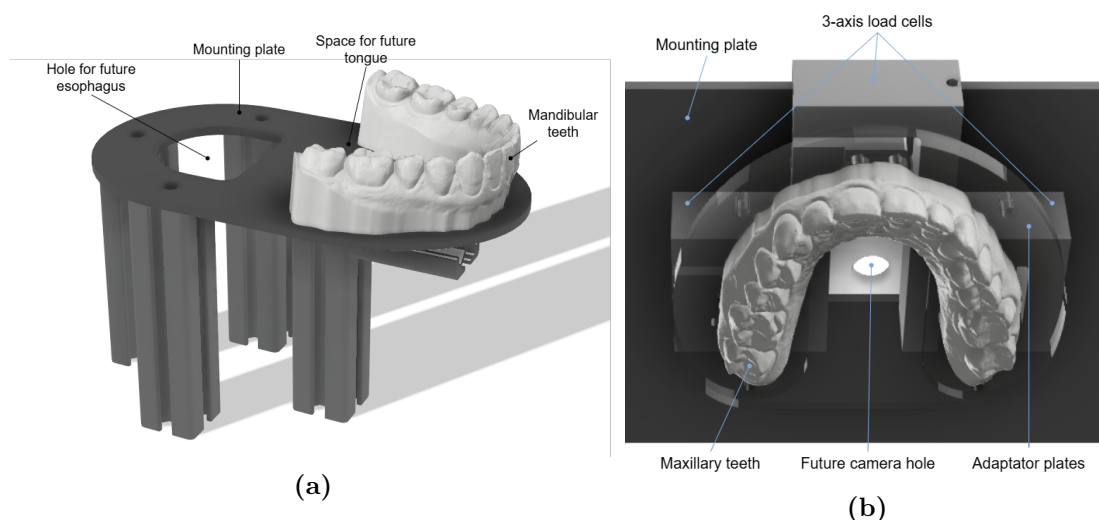


Figure 4: (a) Annotated lower jaw design. (b) Annotated upper jaw design.

2.2.4 Full assembly

Final workspace. The final design is shown in Figure 5a. The height of the upper jaw subsystem was set slightly below the platform’s maximum vertical reach—roughly centered in the middle of its vertical workspace. This positioning ensures that the robot can apply maximum vertical force when the mandibular and maxillary teeth are in contact, while still allowing enough range to meet angular requirements during chewing. A detailed view of the vertical workspace

can be found in Figure 5b. The lateral and anterior-posterior workspaces are constrained by the upper jaw frame and are approximately ± 60 mm and ± 80 mm, respectively. The base is designed as a hollow box to house the electronics described in Section 2.3.

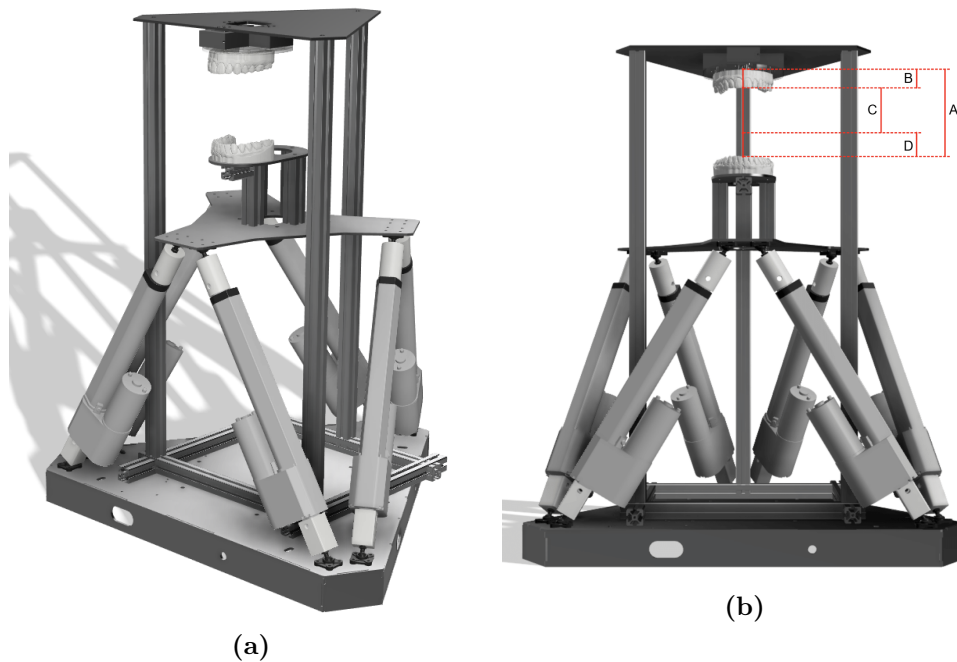


Figure 5: (a) Final design overview. (b) Workspace design: A-Full vertical workspace of 118 mm; B-Upper margin of 25 mm; C-Working chewing volume of 60 mm; D-Bottom margin of 33 mm.

Material selection. The base, platform, lower jaw mount, and upper jaw mount are all made out of steel, see Table 3. Although heavier than aluminum, steel offers significantly higher stiffness, with a Young’s modulus of 190-210 GPa. This makes it a better choice for components that require high rigidity and minimal deformation under load. Additionally, steel’s weldability makes it practical for future modifications—for example, adding reinforcement ribs to the upper jaw mounting plate to further improve structural stability.

Subassembly	Part	Material
Stewart Platform	Base	Steel
	Platform	Steel
	Adaptator	PLA
Lower Jaw	Lower jaw mounting plate	Steel
	Mandibular teeth	PLA
Upper Jaw	Upper jaw mounting plate	Steel
	Upper jaw adaptator plates	Acrylic
	Maxillary teeth	PLA

Table 3: Mechanical design materials.

Waterproofing. As the robot is designed to eventually include a saliva module, it is important to ensure that the electronics and mechanical components are protected from moisture. First,

we protected the steel parts with a layer of paint to prevent rusting. Then on both the upper and bottom side of the base, a plastic sheet was added to isolate the electronics from the steel base and prevent water from entering inside the box and damaging the electronics. Finally, the linear actuators are IP54 rated, meaning they are protected against dust and splashes of water from any direction, see Table 2.

Specifications summary. The final specifications of the chewing robot are summarized in Table 4. It is worth noting that the center of mass height is expected to decrease further once the electronic components are installed within the base enclosure.

Parameter	Value
Total mass	21 kg
Dimensions (L x W x H)	530 mm x 460 mm x 600 mm
Center of mass	150 mm above base center
Vertical force capacity ($F_{z,\max}$)	1155 N
Lateral force capacity ($F_{x,\max}$)	444 N
Anterior-posterior force capacity ($F_{y,\max}$)	385 N
Vertical workspace	118 mm
Lateral workspace	± 60 mm
Anterior-posterior workspace	± 80 mm
Working vertical chewing volume	60 mm
Actuator stroke length	101 mm
Max actuator speed (no load)	28 mm/s
Max actuator speed (full load)	21 mm/s
Moisture protection	Painted + plastic sheets + IP54-rated actuators

Table 4: Final specifications of the chewing robot.

2.3 Control

This section describes the hardware and software architecture of the chewing robot as well as the control strategy.

2.3.1 Hardware (electronics)

A Teensy 4.1 (600 MHz ARM Cortex-M7, single-precision FPU) executes the control loop. Its key peripherals are:

- three 12 A dual DC motor drivers (DF Robot) controlling the six linear actuators;
- six analogue inputs reading potentiometer position feedback from the linear actuators;
- three transmitters for the load cells mounted on top of the maxilla;
- an on-board micro-SD slot used for trajectory files and calibration data.

A 12 V AC/DC brick powers the actuators directly; the user’s computer supplies 5 V to the Teensy, which in turn sources the 3.3 V logic rails for the motor drivers and load-cell transmitters. The full electronics schematic is shown in Fig. 6.

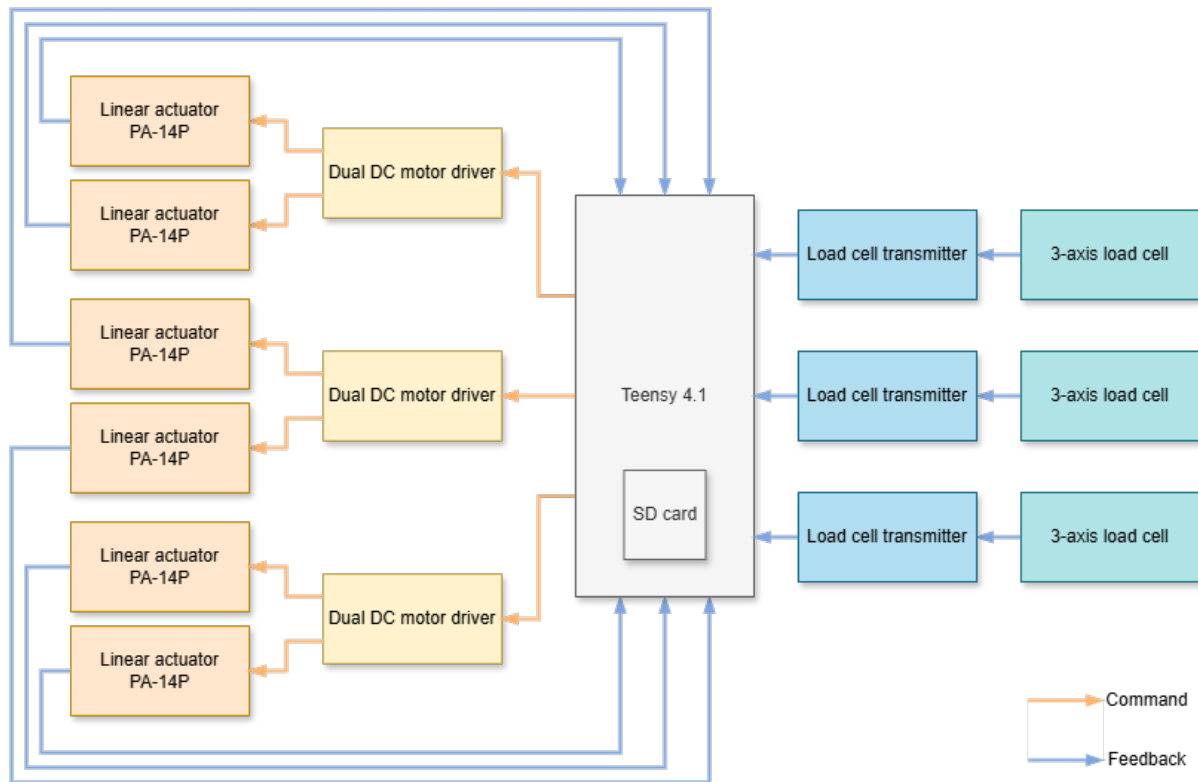


Figure 6: Electronics schematic.

2.3.2 Software architecture

The central class `RobotController` maintains the finite-state machine in Fig. 8 and manages two modules:

- **StewartPlatform**: inverse kinematics, trajectory interpolation, and low-level actuator commands;
- **ForceSensing**: continuous load-cell acquisition and filtering;

The controller is designed to be modular, allowing for easy addition of new modules such as a tongue or saliva module in the future. The three controller states are:

1. **Stop** – return to home pose; reload trajectory if the user selects a new file;
2. **Calibrate** – user can manually change the initial (x, y, z) position via the GUI;
3. **Move** – replay the selected trajectory.

A lightweight Python GUI on the host PC issues high-level commands, such as state changes, and plots sensor data.

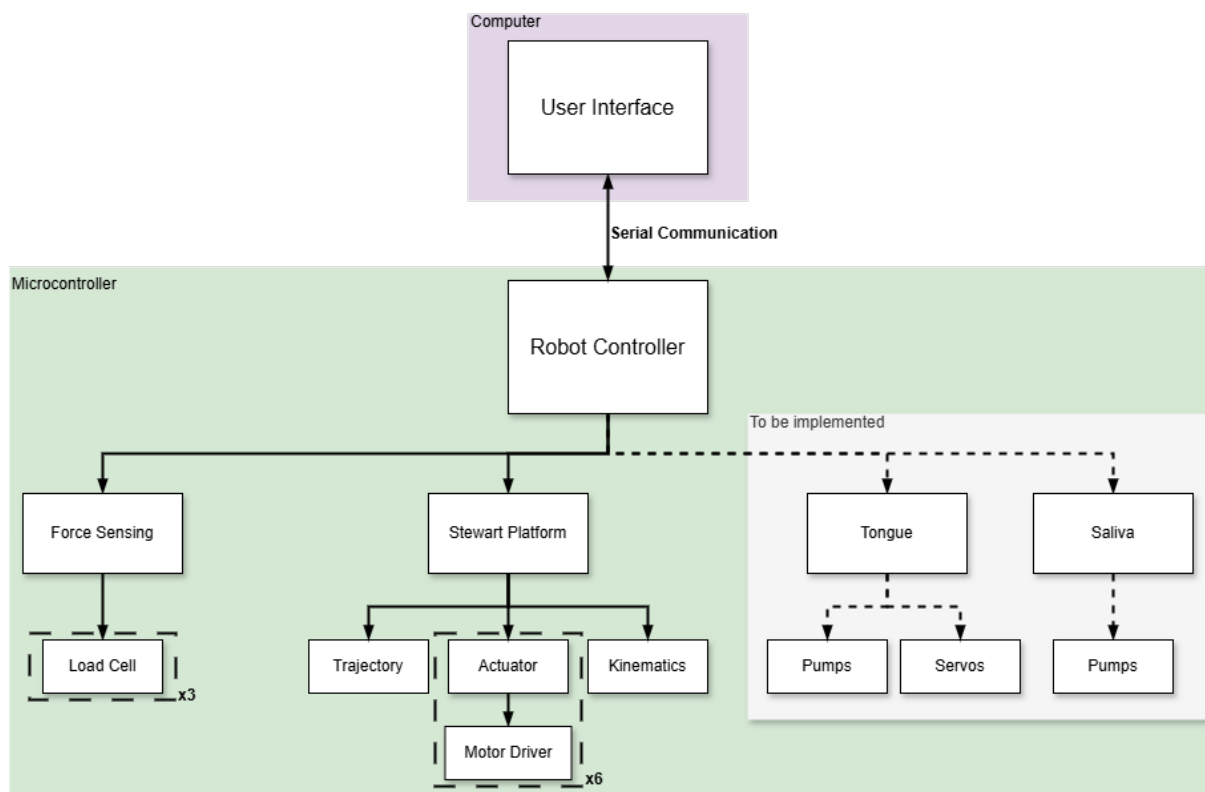


Figure 7: Overall code structure.

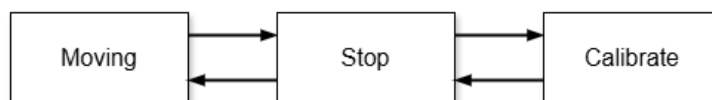


Figure 8: Robot controller state machine.

2.3.3 Stewart platform control

The Stewart platform is controlled by the `StewartPlatform` class, which manages The Stewart Platform follows a 3D trajectory (x, y, z , roll, pitch, yaw) from a .csv file on the micro-SD card. See section 2.4 for details on the recording protocol and data processing. Each pose is defined by its position $\mathbf{t} = (x, y, z)$ and orientation given by the Euler angles (ϕ, θ, ψ) , which are the roll, pitch, and yaw angles respectively. The trajectory is then linearly interpolated with a fixed time step chosen by the user.

Inverse kinematics For each pose in the trajectory, `Kinematics` computes the lengths of the six linear actuators that will achieve the desired pose of the platform, i.e. the inverse kinematics. First, let's define our system. The base is defined as the global reference frame with orthogonal axes (x, y, z), while the platform is associated with a local orthogonal coordinate system (x', y', z'). Figure 9 shows a visualization of these axes. The platform has six degrees of freedom relative to the base: three translational and three rotational. To account for the platform's rotation, we use the standard rotation matrix $R(\phi, \theta, \psi)$, which is defined as the product of three rotation

matrices about the Z , Y , and X axes:

$$R(\phi, \theta, \psi) = R_Z(\psi)R_Y(\theta)R_X(\phi) = \begin{pmatrix} \cos \psi & -\sin \psi & 0 \\ \sin \psi & \cos \psi & 0 \\ 0 & 0 & 1 \end{pmatrix} \begin{pmatrix} \cos \theta & 0 & \sin \theta \\ 0 & 1 & 0 \\ -\sin \theta & 0 & \cos \theta \end{pmatrix} \begin{pmatrix} 1 & 0 & 0 \\ 0 & \cos \phi & -\sin \phi \\ 0 & \sin \phi & \cos \phi \end{pmatrix}$$

In our case, the center of rotation is the gnathion, defined as a fixed point \mathbf{c} , rather than the origin of the platform. Therefore, the platform joints \mathbf{p}_i , i being the actuator index, are first rotated about the gnathion and then translated by the user-defined home position $\mathbf{T} = (x, y, z)$, resulting in the global coordinates of the platform joints:

$$\mathbf{q}_i = R(\mathbf{p}_i - \mathbf{c}) + \mathbf{c} + \mathbf{T}.$$

Figure 10 shows the kinematic schematic for the i^{th} actuator. Finally, the actuator length is the Euclidean distance to the fixed base joint \mathbf{b}_i :

$$\ell_i = \|\mathbf{q}_i - \mathbf{b}_i\|_2.$$

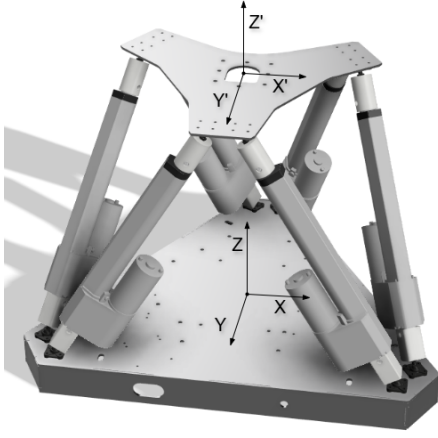


Figure 9: Robot referential.

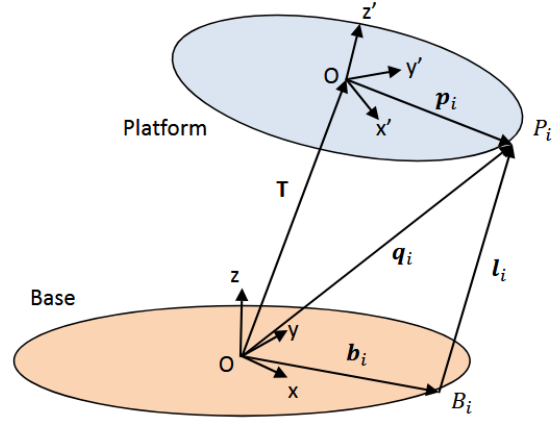


Figure 10: Schematic of the Stewart platform kinematics for the i^{th} actuator [10].

PI controller For each actuator, its desired length is sent to a PI position controller, see Figure 11. The PI gain values are set to $K_P = 25$ and $K_I = 0.1$, which were determined empirically to achieve a good trade-off between responsiveness and stability. An anti-windup mechanism is implemented to prevent the integral term from growing too large, which could lead to overshooting. To minimize the noise of the potentiometer feedback, we apply a low-pass filter averaging the last 10 samples.

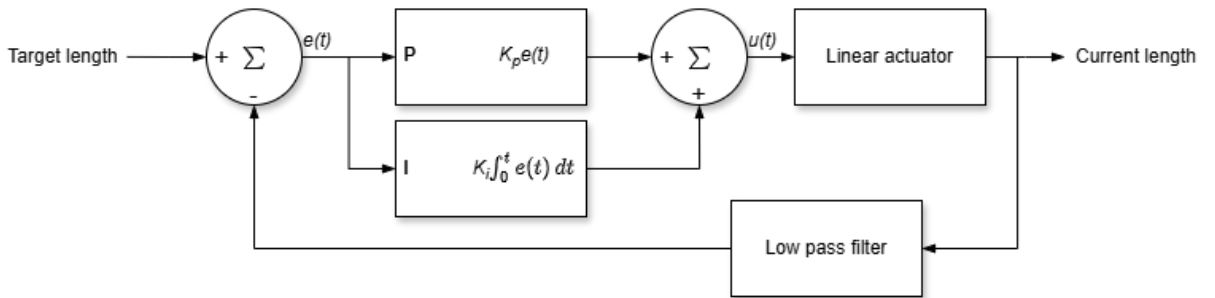


Figure 11: Position PI controller for the linear actuators.

2.3.4 Force sensing

The **ForceSensing** module is responsible for acquiring and processing data from the three tri-axial load cells mounted on the upper jaw. Each load cell is represented by an instance of the **LoadCell** class, which performs signal conditioning on the raw sensor data. Specifically, a low-pass filter is applied by averaging the last 10 samples to reduce high-frequency noise.

According to the manufacturer's calibration data, the load cell output from the transmitter is sufficiently linear for direct mapping (Figure 12). Based on this, the **LoadCell** class linearly scales the filtered signal to a calibrated force range of [0, 500] N. To eliminate static bias introduced by preloading or assembly stress, each load cell is automatically tared at system startup.

The **ForceSensing** module aggregates the force data from all three load cells to compute the total force applied on the upper jaw. Since each load cell only measures force in the positive direction of its axis, their physical orientation must be accounted for during summation. This configuration is illustrated in Figure 13. The total forces in the x, y, and z directions are calculated as:

$$F_{x,total} = F_{x,front} + F_{x,backL} - F_{x,backR}, \quad (5)$$

$$F_{y,total} = F_{y,front} + F_{y,backL} - F_{y,backR}, \quad (6)$$

$$F_{z,total} = F_{z,front} + F_{z,backL} + F_{z,backR}. \quad (7)$$

For now, the **ForceSensing** module primarily serve as a safety mechanism. If the total measured force exceeds predefined thresholds—200 N in the z-direction, 60 N in x, or 50 N in y—the module fails and triggers **RobotController** to transition to **Stop** mode to prevent damage to the robot.

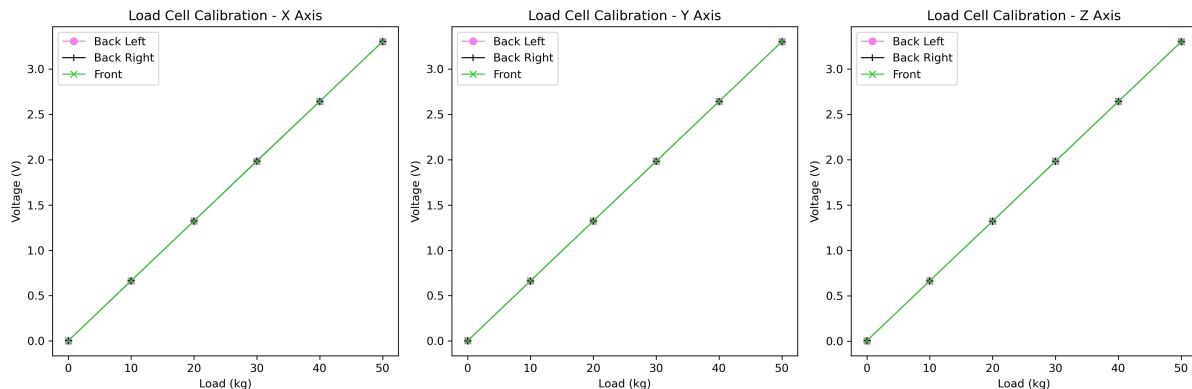


Figure 12: Load cell calibration data.

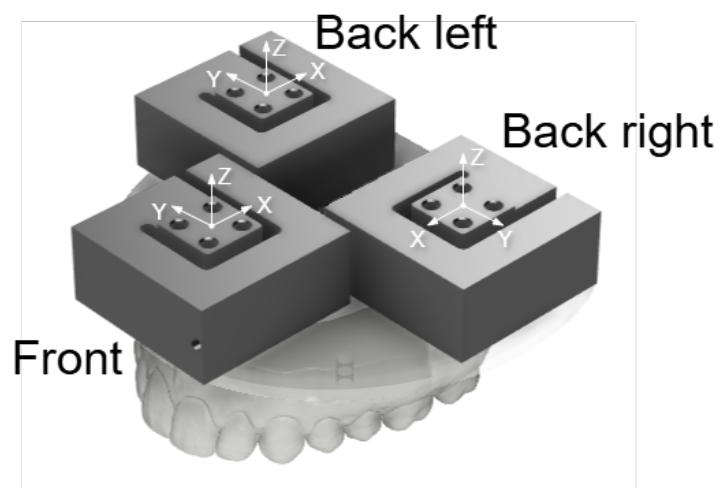


Figure 13: Load cells orientation.

2.4 Data acquisition and processing

2.4.1 Subjects

Two healthy adult volunteers (author and project supervisor) participated in this pilot recording. Informed consent was obtained from both participants. Owing to time constraints and the exploratory nature of the study, no additional subjects were recruited.

2.4.2 Motion-capture acquisition

Mandibular motion was recorded with a five-camera OptiTrack system sampling at 120 Hz. Four reflective markers arranged in a square were attached to the forehead and served as a head-fixed reference frame. A second set of three markers forming a triangle was placed on the gnathion. Two additional lip markers were recorded but later discarded because a single marker cannot encode orientation. [11, 12]

The subject then performed the motion sequences listed in Table 5. Each frame was saved by Motive as a .csv file that contains the 3-D marker positions (in millimetres) and the orientation of each marker set as quaternions. The calibrated volume had a residual error of 0.3 mm.

Food	Motion	Optional: Duration
Empty mouth	20× open–close cycles	—
Chewing gum (Xylit-Pro, <i>Excitemint</i>)	Random side chewing	2 min
	Right-side chewing	1 min
	Left-side chewing	1 min
	Front-teeth-only chewing	1 min
Biscuits (Bretzeli, <i>Kambli</i>)	random chewing	—
	front-teeth chew → right-side chew	—
	front-teeth chew → left-side chew	—
	<i>fast</i> random chewing	—
	<i>slow</i> random chewing	—

Table 5: Recording protocol. *Notes:* For chewing-gum trials the first run began with an unchewed piece and the same gum was kept for all subsequent motions. For biscuit trials each run started with an empty, closed mouth; the subject then placed a biscuit, chewed as instructed, and swallowed.

2.4.3 Data processing

To reduce high-frequency noise in the motion capture data, a 4th-order Butterworth low-pass filter was applied, with a cutoff frequency set at 6 Hz. This value was chosen based on reported human mastication frequencies, typically ranging from 1-3 Hz and up to 6 Hz when the subjects are instructed to chew at higher rates [13].

Following filtering, the gnathion marker motion was transformed to the head-fixed marker reference frame using rotation matrices, effectively compensating for head motion during recording. The next step was to convert the data into the robot’s coordinate system, defined as follows:

- the X axis is horizontal, pointing to the subject’s left;
- the Y axis is horizontal, pointing forward;
- the Z axis is vertical, pointing upwards.

Due to uncertainty about the absolute orientation of the OptiTrack coordinate system, we performed Principal Component Analysis (PCA) on the recorded open-close cycles to estimate the appropriate rotation matrix. The underlying assumption is that the largest motion range (i.e., the first principal component) corresponds to the robot’s Z -axis, the second to the Y -axis, and the third to the X -axis, following the hierarchy of motion amplitude typical in mastication dynamics during mouth opening [14]. As the principal components (PC) are orthogonal, the resulting matrix forms a valid orthonormal basis. The rotation matrix is then constructed by assigning the principal components as its column vectors.

Upon visual inspection of the data, we flipped the Y and Z axes so that both decrease during jaw opening, ensuring alignment with the robot’s coordinate conventions. All positional and rotational data were then projected into this new reference frame using the resulting rotation matrix:

$$R = \begin{pmatrix} \text{PC}_1 & -\text{PC}_2 & -\text{PC}_3 \end{pmatrix}.$$

To express orientation, the recorded quaternions were converted to Euler angles, providing the roll, pitch, and yaw components used by the robot’s Stewart platform.

Then, to align the trajectory with the robot’s origin, positional and rotational offsets were com-

puted from the final stationary segment of the recording. The last second of the dataset—during which the subject remained still—was used to compute the median values of position and orientation. These offsets were subtracted from the full dataset to ensure proper alignment with the robot’s neutral pose.

Finally, the most suitable trajectory segments were selected for replay on the robot. Selection was based on the smoothness of motion and the absence of outliers or artifacts in the recorded data.

3 Results

3.1 Mimicking human jaw motion

- human jaw motion from motion capture
- results of PCA on human jaw motion
- show graphs of human jaw motion vs robotic jaw motion
- show graphs of the force during chewing for human vs robot

3.2 Motion captured chewing trajectories

3.3 Position control

Speed and accuracy To evaluate the performance of the position control system, we investigated the robot’s ability to track a predefined trajectory at varying speeds. In this context, “speed” refers to the time interval between consecutive trajectory points. While the motion capture data was recorded at 120 Hz (approximately every 8.3 ms), the playback was tested at longer intervals: 40 ms (25 Hz), 50 ms (20 Hz), 60 ms (16.67 Hz), 70 ms (14.29 Hz), 80 ms (12.5 Hz), 90 ms (11.11 Hz), and 100 ms (10 Hz).

For this test, a 10-second segment of randomly selected chewing motion was used. We recorded both the target and actual actuator lengths across all actuators. Figure 15 illustrates the tracking performance of actuator 2 at the various speeds. To quantify timing discrepancies, we conducted a cross-correlation analysis between the target and actual actuator lengths, providing both time delays (Figure 15) and cross-correlation coefficients (Figure 16).

The results show that at a sampling interval of 100 ms (10 Hz), the robot tracks the trajectory well, with an average delay of 0.7 s and cross-correlation coefficients exceeding 0.975. However, performance degrades significantly at higher speeds (i.e., shorter intervals), as reflected in both increased delays and a drop in correlation values—especially below 80 ms, where the tracking error becomes pronounced and key trajectory peaks are missed.

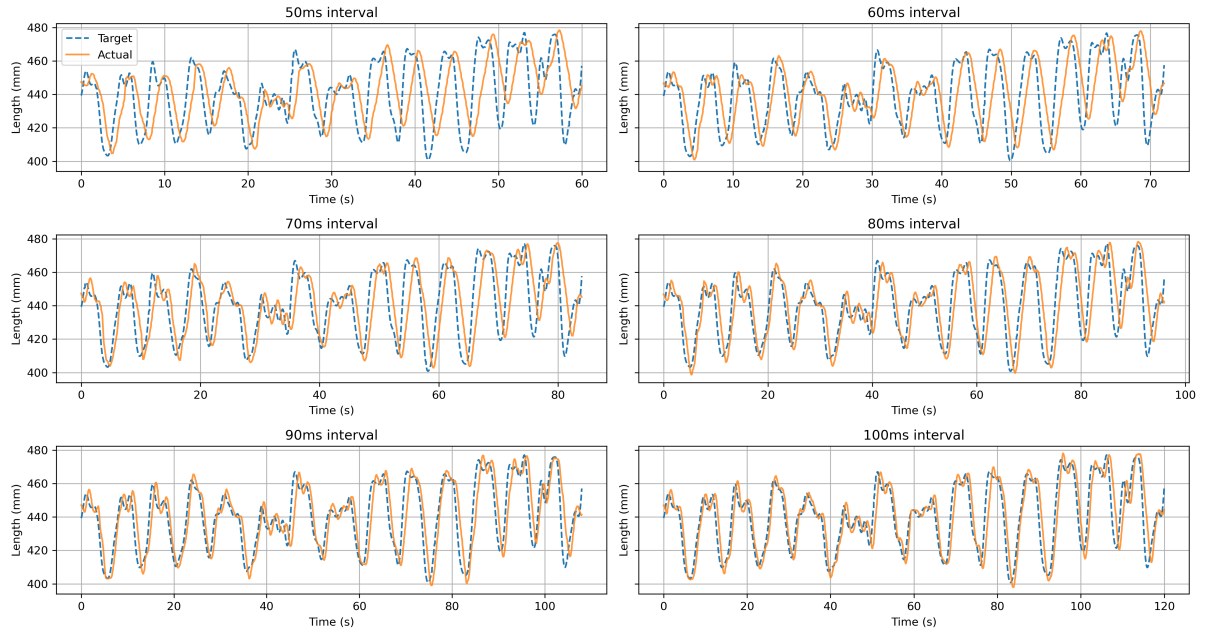


Figure 14: Performance of position control of actuator 2 across different time intervals between trajectory points.

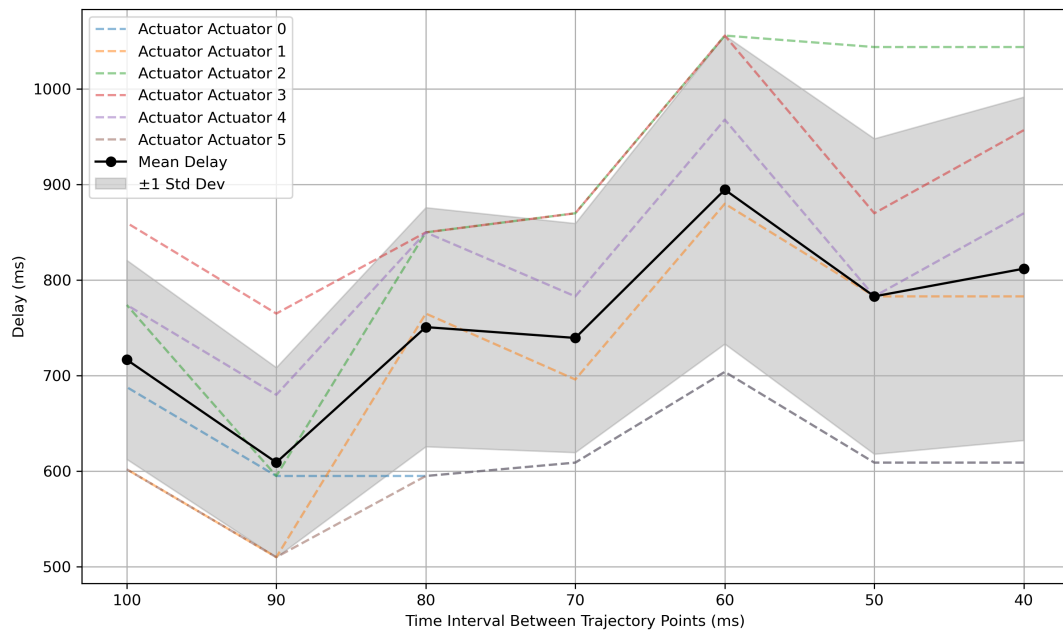


Figure 15: Delays between target and actual actuator length across different time intervals.

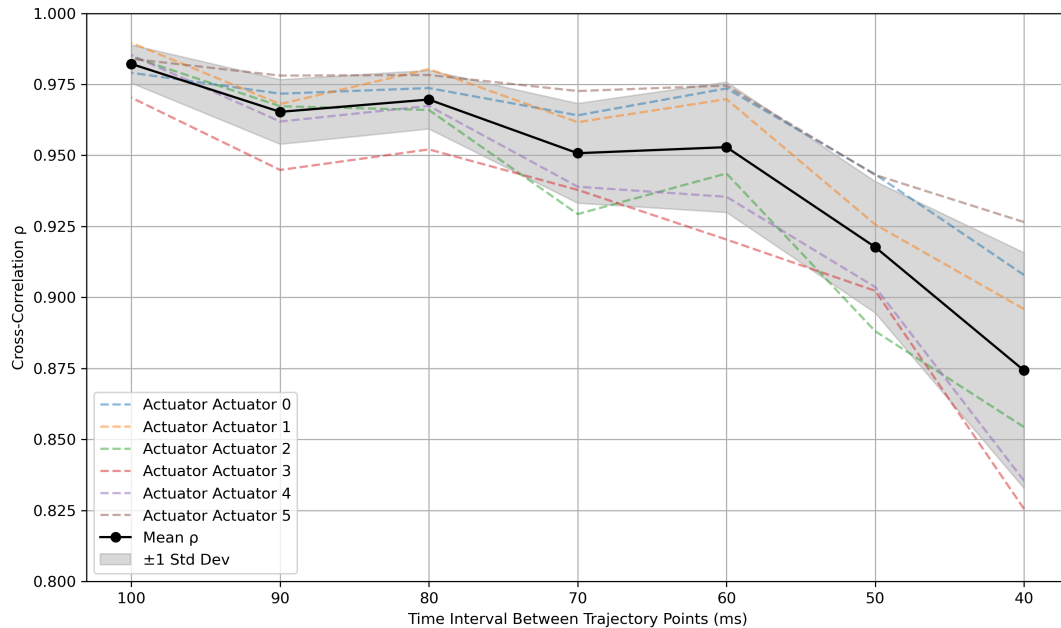


Figure 16: Cross-correlation coefficients across actuators for different time intervals.

3.4 Force analysis

3.4.1 Maximum force

The robot’s vertical force generation capabilities were assessed using manual control mode normally used to set the robot’s home position during calibration. The platform was driven at its highest height under active force feedback while avoiding structural failure. The upper bound of the robot’s vertical force output was constrained by the stiffness of the upper jaw structure, which visibly bent under high vertical force. table 6 shows the maximum forces recorded by the three load cells during this test, see Figure 13. for the load cell positions. The results shows that most of the vertical force is applied on the back load cells, which reflects the anatomical load pattern during full occlusion, where the molars bear the majority of chewing forces. The total vertical force output of the robot is 315.98 N, which is well within the average occlusal force during chewing, although below the maximum bit force from Table 1.

Load Cell	$F_{z,max}$ (N)	$F_{y,max}$ (N)	$F_{x,max}$ (N)
Back Right Load Cell	124.63	x	x
Back Left Load Cell	124.63	x	x
Front Load Cell	66.28	x	x
Total Force	315.98	x	x

Table 6: Maximal forces recorded by the load cells during the force test.

3.4.2 Force feedback distribution

To evaluate the spatial resolution of the force sensing system, we applied a simple vertical trajectory while placing a piece of gum-like material at three distinct positions between the

teeth: back right, front, and back left. The vertical force output from each of the three load cells was recorded (Figure 17).

The plot clearly shows three distinct peaks corresponding to the three test positions, confirming the system’s capability to localize force application across the dental arch. Additionally, when force is applied at the back, the front load cell registers a smaller secondary response. This is consistent with the mechanical coupling in the mounting structure, as the front load cell is physically situated between the two rear ones.

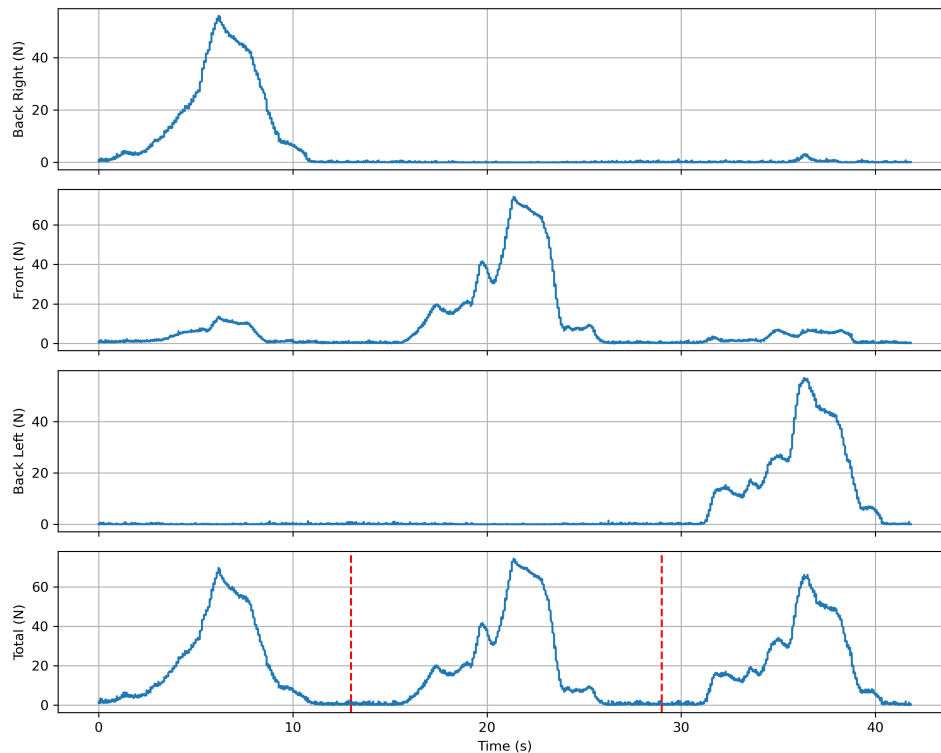


Figure 17: Vertical force output across three load cells during chewing with localized gum placement. The red lines separate the three gum positions: back right, front, and back left.

4 Discussion

4.1 Summary of findings

4.2 Limitations

- So far very big and heavy robot due to steel plates and big actuator \neq human jaw
- 3D printed teeth/jaw not strong enough to withstand the forces applied by the actuators

4.3 Future work

- 3D printed jaw/teeth to be replaced by a more rigid material
- add a tongue module
- add a saliva module

- adapt state machine to coordinate the different modules
- add a camera to track the food

5 Conclusion

6 References

- [1] K Alemzadeh and D Raabe. “Prototyping artificial jaws for the Bristol Dento-Munch Robo-Simulator; ‘A parallel robot to test dental components and materials’”. English. In: (2007). ISBN: 9781424407873 Name and Venue of Conference: 29th Annual International Conference of the IEEE Engineering in Medicine and Biology Society - Lyon, France Conference Organiser: IEEE, EMBS, SFGBM, pp. 1453–1456. DOI: [10.1109/IEMBS.2007.4352574](https://doi.org/10.1109/IEMBS.2007.4352574).
- [2] Seung-Ju Lee et al. “Design of mastication robot with life-sized linear actuator of human muscle and load cells for measuring force distribution on teeth”. In: *Mechatronics* 51 (2018), pp. 127–136. ISSN: 0957-4158. DOI: <https://doi.org/10.1016/j.mechatronics.2017.11.013>. URL: <https://www.sciencedirect.com/science/article/pii/S0957415817301769>.
- [3] Kazem Alemzadeh et al. “Development of a Chewing Robot with Built-in Humanoid Jaws to Simulate Mastication to Quantify Robotic Agents Release from Chewing Gums Compared to Human Participants”. English. In: *IEEE Transactions on Biomedical Engineering* 68.2 (Feb. 2021), pp. 492–504. ISSN: 0018-9294. DOI: [10.1109/TBME.2020.3005863](https://doi.org/10.1109/TBME.2020.3005863).
- [4] Johannes H. Koolstra. “Dynamics of the Human Masticatory System”. In: *Critical Reviews in Oral Biology & Medicine* 13.4 (2002), pp. 366–376. ISSN: 1045-4411. DOI: [10.1177/154411130201300406](https://doi.org/10.1177/154411130201300406). URL: <https://doi.org/10.1177/154411130201300406>.
- [5] K.C. Julien et al. “Normal masticatory performance in young adults and children”. In: *Archives of Oral Biology* 41.1 (1996), pp. 69–75. ISSN: 0003-9969. DOI: [https://doi.org/10.1016/0003-9969\(95\)00098-4](https://doi.org/10.1016/0003-9969(95)00098-4). URL: <https://www.sciencedirect.com/science/article/pii/0003996995000984>.
- [6] Charles H. Gibbs et al. “Maximum clenching force of patients with moderate loss of posterior tooth support: A pilot study”. In: *The Journal of Prosthetic Dentistry* 88.5 (2002), pp. 498–502. ISSN: 0022-3913. DOI: <https://doi.org/10.1067/mpr.2002.129062>. URL: <https://www.sciencedirect.com/science/article/pii/S0022391302002585>.
- [7] Sarah C. Woodford et al. “Muscle and joint mechanics during maximum force biting following total temporomandibular joint replacement surgery”. In: *Biomechanics and Modeling in Mechanobiology* 23.3 (2024), pp. 809–823. ISSN: 1617-7959. DOI: [10.1007/s10237-023-01807-1](https://doi.org/10.1007/s10237-023-01807-1). URL: <https://doi.org/10.1007/s10237-023-01807-1>.
- [8] Vassil Svechtarov et al. “Mandibular range of motion and its relation to temporomandibular disorders”. In: *Scripta Scientifica Medicinæ Dentalis* 1.1 (2015).
- [9] Oren Masory and Jian Wang and. “Workspace evaluation of Stewart platforms”. In: *Advanced Robotics* 9.4 (1994), pp. 443–461. DOI: [10.1163/156855395X00508](https://doi.org/10.1163/156855395X00508). eprint: <https://doi.org/10.1163/156855395X00508>. URL: <https://doi.org/10.1163/156855395X00508>.
- [10] Unknown. *DIY Stewart Platform*. 2024. URL: <https://cdn.instructables.com/ORIG/FFI8ZXW/I55MMY14/FFI8ZXWI55MMY14.pdf>.
- [11] Steven Mills et al. “Principal Component Representations of Chewing Motion”. In: IVCNZ ’14 (2014), pp. 218–223. DOI: [10.1145/2683405.2683434](https://doi.org/10.1145/2683405.2683434). URL: <https://doi.org/10.1145/2683405.2683434>.
- [12] Meg Simione et al. “Differing structural properties of foods affect the development of mandibular control and muscle coordination in infants and young children”. In: *Physiology & Behavior* 186 (2018), pp. 62–72. ISSN: 0031-9384. DOI: <https://doi.org/10.1016/j.physbeh.2018.01.009>. URL: <https://www.sciencedirect.com/science/article/pii/S0031938418300155>.

- [13] T. Morimoto et al. “Frequency-dependent Modulation of Rhythmic Human Jaw Movements”. In: *Journal of Dental Research* 63.11 (1984). PMID: 6594375, pp. 1310–1314. DOI: [10.1177/00220345840630111201](https://doi.org/10.1177/00220345840630111201).
- [14] K.H. Travers et al. “Associations between incisor and mandibular condylar movements during maximum mouth opening in humans”. In: *Archives of Oral Biology* 45.4 (2000), pp. 267–275. ISSN: 0003-9969. DOI: [https://doi.org/10.1016/S0003-9969\(99\)00140-5](https://doi.org/10.1016/S0003-9969(99)00140-5). URL: <https://www.sciencedirect.com/science/article/pii/S0003996999001405>.

7 Appendix